Particle & Particle Systems Characterization
www.particle-journal.com

Assembly of Zinc-Single-Site-Containing Silica Nanoparticles to Supraparticle Powders with Destructibility to Serve as Filler and Vulcanization Activator in Rubbers

Sarah Wenderoth, Paola Milana, Thomas Zimmermann, Moritz Deues, Maximilian Oppmann, Johannes Prieschl, Silvia Mostoni, Roberto Scotti, Susanne Wintzheimer, and Karl Mandel**

The vulcanization process is widely used in industry for tire manufacturing. Therefore, zinc oxide is commonly utilized as an activator material, but unreacted zinc oxide remains in the final products and can be released into the environment with a significant impact. To reduce the amount of required zinc and to prevent leaching from tire material, zinc single site-containing silica fillers are interesting candidates. In these materials, zinc sites are anchored on the surface of silica nanoparticles through their complexation with functionalized aminosilanes. Based on these, a novel powder sample is prepared via spray-drying. The obtained supraparticles allow for a homogeneous distribution of the filler nanoparticles in the rubber matrix via their disintegration during the incorporation process. All synthesis steps are carried out in ethanol and water, respectively, at very mild temperatures to account for sustainability demands. As core of this study, the role of zinc ions and their amino-complexation in nanoparticle dispersion stability and in supraparticle formation during spray-drying is elucidated. Additionally, the superior performance of supraparticles as activator in rubber vulcanization is demonstrated. These show a higher curing efficiency, leading to lower curing time (−70%), higher torque values (+15%), and improved dynamic mechanical properties compared to the conventional ZnO activator.

1. Introduction

In the European Union alone, more than 4 million tons of tires have been manufactured annually over the past 20 years.[1] They are all produced by adding reinforcing fillers such as silica, silicates, or carbon black to the rubber to form percolating networks within the rubber nanocomposites. Furthermore, a vulcanization process is carried out for curing to impart the desired mechanical properties.[2] During this process, sulfur reacts with rubber molecules at relatively high temperatures (140–170 °C) to form chemical bonds and create a 3D network within the rubber matrix.[3] In order to increase the curing efficiency, the reaction is often accelerated by the addition of accelerators, activators, and co-activators, such as benzothiazoles, zinc oxide, and fatty acids such as stearic acid.[4] Zinc, in particular, ZnO, is the traditional industrially employed vulcanization activator and a promising candidate for electrochemical and photochemical applications.[5] However, since the various zinc complexes formed during the vulcanization mechanism and unreacted ZnO remain in the final product,[6] it is necessary to reduce its amount for sustainability reasons: Zinc is toxic to aquatic organisms and enters the environment during tire manufacturing, degradation, and recycling as well as through tire abrasion and leaching during use.[7] There are currently diverse approaches addressing this issue[6] that include the size reduction of the zinc-based activators,[8] the

S. Wenderoth, M. Deues, M. Oppmann, S. Wintzheimer, K. Mandel
Fraunhofer Institute for Silicate Research
Neunerplatz 2, 97082 Würzburg, Germany
E-mail: susanne.wintzheimer@isc.fraunhofer.de; karl.mandel@fau.de

The ORCID identification number(s) for the author(s) of this article can be found under https://doi.org/10.1002/ppsc.202300161

DOI: 10.1002/ppsc.202300161

P. Milana, S. Mostoni, R. Scotti
Department of Materials Science
INSTM
University of Milano Bicocca
Via Roberto Cozzi 55, Milano 20125, Italy

T. Zimmermann, J. Prieschl, S. Wintzheimer, K. Mandel
Department of Chemistry and Pharmacy
Friedrich-Alexander-Universität Erlangen-Nürnberg
Egerlandstraße 1, 91058 Erlangen, Germany

R. Scotti
Institute for Photonics and Nanotechnologies-CNR
Via alla Cascata 56/C, Povo (TN) 38123, Italy

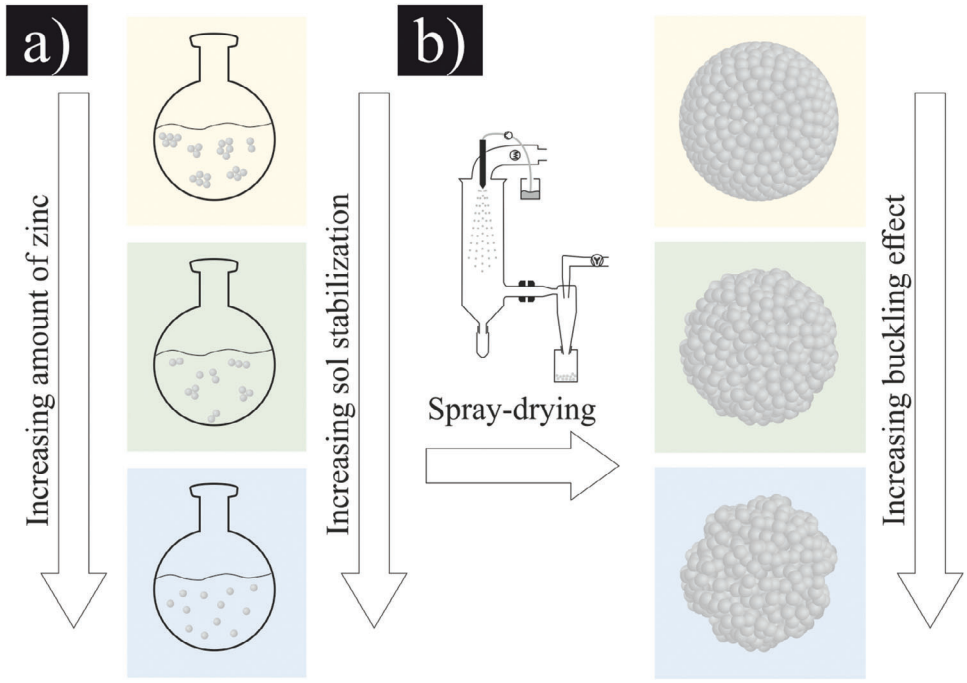

Scheme 1. As the zinc concentration increases, a) the stability of the nanoparticle dispersion inclines, b) leading to more buckled supraparticles during spray-drying.

introduction of reactive zinc complexes,[9] the use of supported zinc-based species with higher dispersion,[10] binary systems or other metal oxides,[11] and even the addition of unusual compounds such as ionic liquids aiming for increased Zn dispersion and availability in rubber compounds.[12] In this context, some of the authors have already demonstrated that ZnO nanoparticles, as well as Zn(II) single sites, can be anchored to the surface filler material (usually silica nanoparticles), obtaining highly reactive dual-function fillers that act simultaneously as reinforcing filler and curing activator (ZnO@SiO_2 and Zn@SiO_2, respectively).[13,14] In particular, Zn@SiO_2 was prepared by a surface modification of silica nanoparticles with an aminosilane (3-aminopropyltriethoxysilane, APTES). Subsequently, Zn(II) single sites were coordinated through the exposed amino groups, where one zinc atom is complexed by two APTES molecules on (only) the same silica nanoparticle. Moreover, compared to the conventionally used powdered ZnO, this approach was able to reduce the total amount of zinc and also to increase the curing efficiency and dynamic mechanical properties of isoprene rubber (IR) nanocomposites used as a classical industrial vulcanization model reaction.[13,15]

Based on this background, the current work aimed to investigate the influence of the filler morphology used to obtain Zn@SiO_2 on the distribution of zinc active sites in the rubber composites and the resulting curing efficiency, as well as their mechanical properties. For this purpose, the functionalized Zn@SiO_2 nanoparticles were arranged in new micrometer-sized units, so-called supraparticles,[16] by exploiting a different drying procedure, i.e., by replacing the classical oven treatment with a spray-drying approach. This fast and industrially scalable process dries the nanoparticle dispersion while simultaneously forcing them together to form supraparticles, avoiding the formation of hard silica agglomerates. The obtained powder sample can be directly used for tire production. Its main advantage is the easy disintegration of the supraparticles under the shear forces applied during their incorporation into the rubber compound, resulting in finely dispersed nanoparticles in the rubber matrix.[17] In this study, Zn@SiO_2 was prepared based on silica nanoparticles – obtained by a classical Stöber process using ethanol as solvent at mild temperatures of 30–40 °C and exploiting sustainable and scalable conditions. Silica nanoparticles were modified with APTES directly in the ethanol-based synthesis mixture at room temperature and the complexation reaction with zinc was carried out in water at room temperature. Finally, the drying process was performed using a spray-dryer to convert the aqueous nanoparticle dispersion into a supraparticulate powder.

During nanoparticle functionalization and supraparticle preparation, correlations between the morphology of the supraparticles (especially their sphericity) and the properties of the nanoparticles in dispersion (agglomeration behavior, viscosity, ζ-potential and pH value) as a function of the zinc ion concentration were noticed and therefore investigated in more detail. Interestingly, as the zinc concentration increases, the agglomeration sizes of the nanoparticles decrease (**Scheme 1a**, from the yellow to the blue marked box), which affects the morphology of the resulting supraparticles formed during the spray-drying process (Scheme 1b). The more destabilized the nanoparticles are, the more spherical the resulting supraparticles remain (yellow marked box), and conversely, the more stable the nanoparticle dispersion is, the more buckled the resulting supraparticles become (blue marked box).

After elucidating the phenomena responsible for both the nanoparticle dispersion and supraparticle properties as the core of this manuscript, the study was concluded by upscaling the

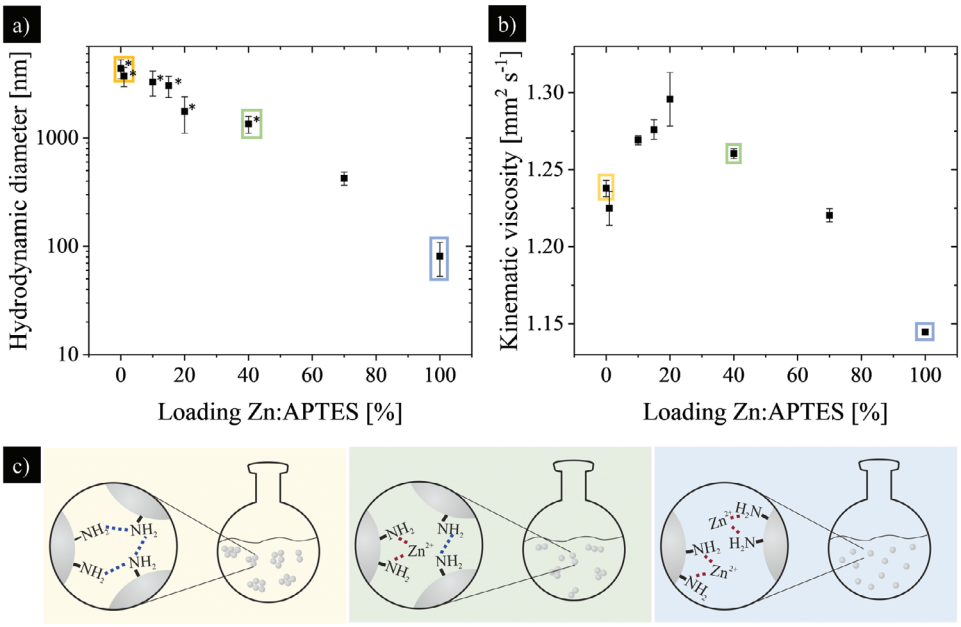

Figure 1. DLS measurements to determine the hydrodynamic diameter a) and measurements of the kinematic viscosity b) of the different silica-APTES-zinc nanoparticle dispersions. Schematic representation of the nanoparticle agglomeration behavior with increasing zinc concentration c) where hydrogen bonds between the amine groups are symbolized with a blue dotted line and the coordination between the amine groups and the zinc atoms are symbolized by red dotted lines. Sample without zinc (yellow), 40% zinc loading (green), and 100% loading (blue) are highlighted. * N.B.: DLS measurements are not accurate for agglomerates above 1000 nm but still indicate dispersion destabilization.

developed synthesis steps and demonstrating their superiority in the vulcanization process of IR nanocomposites compared to benchmark materials.

2. Results

The current work aimed to further improve the findings of Mostoni et al.[13] Compared to this procedure, more sustainable conditions were adopted, by replacing toluene and reflux conditions (120 °C) for the functionalization steps, with green solvents (ethanol and water) and mild temperatures (30–40 °C). Besides, a major change in the synthesis protocol was the use of Stöber silica instead of precipitated silica. This ensures that the nanoparticles are individually present and not agglomerated before the modification step. In addition, the modification of APTES is simplified as it can be carried out directly in the reaction medium and no additional solvent is required.

The synthesis of the silica nanoparticles with a size of 40–50 nm (determined by measuring the hydrodynamic diameter – ESI, part 4) was performed according to the classical Stöber protocol (detailed description in the Materials and Methods section).[18] The subsequent functionalization with APTES (theoretical loading degree of 100% according to the literature[19,20]) was confirmed by thermal gravimetric analysis (TGA, Figure S1, Supporting Information). The quantification of APTES was determined by using calculation models previously published elsewhere.[13] The TGA results indicate the presence of 1.9×10^{-4} mol APTES per 1 g silica, in agreement with the expected theoretical values. The batch (hereafter referred to as silica-APTES) was divided into eight equal parts (each containing 1.5 g of silica). These dispersions were then mixed with zinc nitrate yielding different degrees of zinc loadings equal to 0%, 1%, 10%, 15%, 20%, 40%, 70%, and 100%, where 0% denotes that no additional zinc has been added and 100% means that all APTES molecules are theoretically saturated with zinc. Two APTES molecules coordinate one zinc atom. The maximum yield of coordinated zinc to APTES corresponds to a ratio of 1:2, regardless of the amount of zinc added.[13] The absolute amount of zinc in each sample (hereafter referred to as silica-APTES-zinc-X%) was determined by inductively coupled plasma with optical emission spectroscopy (ICP-OES) measurements and agreed well with the theoretically calculated amounts (Table S1, Supporting Information).

In order to determine the influence of the respective zinc loading on the silica nanoparticle dispersion, they were characterized by dynamic light scattering (DLS), kinematic viscosimetry measurements, and ζ-potential measurements. The DLS measurements provided the hydrodynamic diameters of the samples and thus the agglomeration behavior of the nanoparticles in dispersion. The silica-APTES nanoparticle dispersion shows very high (>4 µm) hydrodynamic diameters indicating that the nanoparticles are highly agglomerated (**Figure 1a**). This agglomeration behavior is presumably caused by hydrogen bondings between the hydrogen atoms of the APTES molecules on the surface of the silica nanoparticles (Figure 1c, yellow box). As the zinc loading increases, the measured particle size decreases. From previous studies, it is known that the zinc atoms are attached to only two APTES molecules, preferably from the same silica nanoparticle, rather than connecting two different nanoparticles, without introducing further inter-nanoparticle bonds. Instead, electrostatic repulsive forces between the zinc atoms counteract thereby the attractive hydrogen bonds between the amine groups and thus

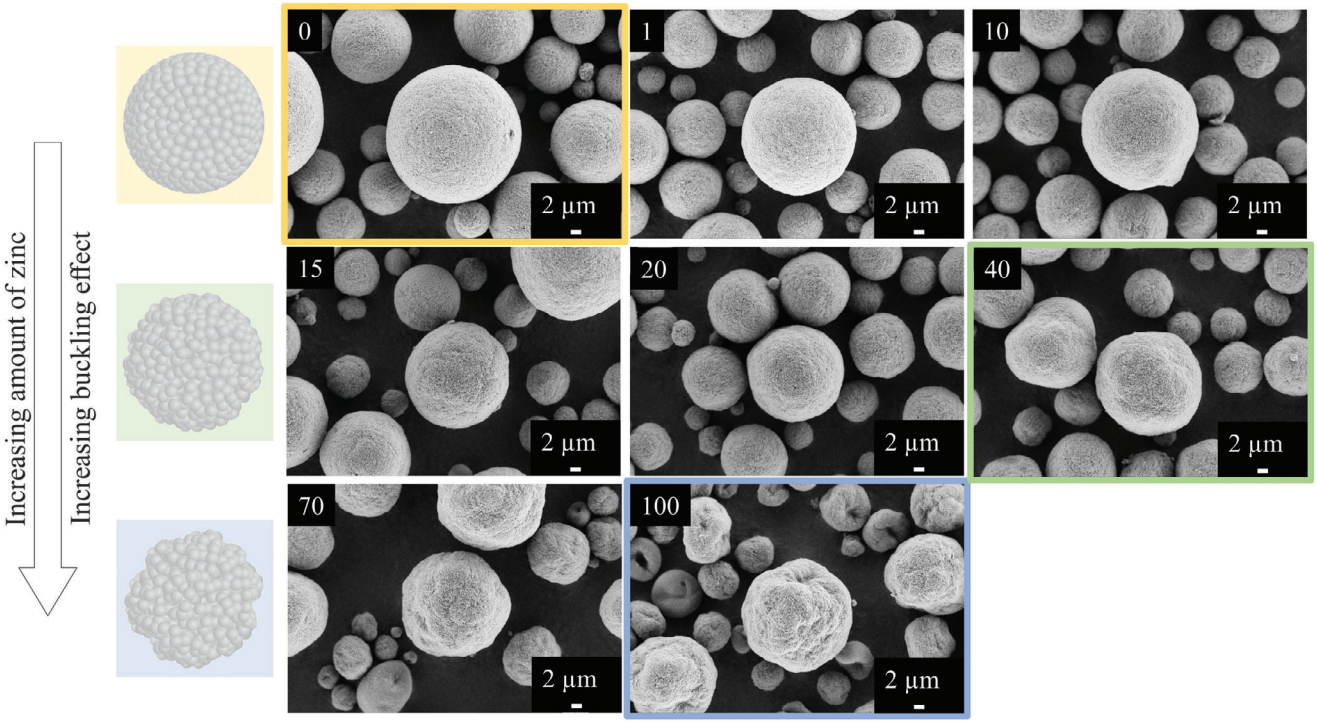

Figure 2. Scanning electron microscopy images of the different supraparticle samples with increasing zinc loading; the top-left-hand-side-corner labels indicate the Zn loading (in percent). The samples without zinc, 40% zinc loading, and full loading are highlighted with yellow, green, and blue frames, respectively.

reduce the inter-nanoparticle attractions (Figure 1c, green to blue box). This ultimately results in electrostatically stabilized dispersions with small agglomerate sizes (i.e., hydrodynamic diameters).

The dispersion properties of the different samples were further investigated by kinematic viscosity measurements (Figure 1b) and complemented by ζ-potential determinations (Figure S2, Supporting Information). At low zinc concentrations, the kinematic viscosities of the dispersions slightly increase compared to the silica-APTES sample, while the negative ζ-potentials shift closer to zero (at the respective pH values between 7 and 8). This shift of the ζ-potentials toward the isoelectric points may cause denser packing of the less-charged single nanoparticles within their agglomerates, resulting in a viscosity increase, while the overall hydrodynamic diameters of the agglomerates do not change (Figure 1a). As the zinc concentration is further increased until the amino groups are completely covered with zinc, the kinematic viscosity (similar to the hydrodynamic diameters in Figure 1a) decreases to a minimum value. In addition, the ζ-potential increases to a value of about +30 mV (at a pH of 6.5) due to the gradual removal of hydrogen bonds and the increase in electrostatic repulsive forces of the zinc ions (Figure 1c, blue box). This results in a reduction of agglomerate sizes (indicated by low hydrodynamic diameters) and thus a stable nanoparticle dispersion, indicated by low viscosity values.

In order to render the nanoparticle dispersion accessible as a rubber additive and vulcanization catalyst, they need to be transformed into a dry powder. Therefore, the spray-drying method was exploited for powder preparation encouraging the supraparticles formation, instead of the traditional drying in an oven. The spray-drying of nanoparticle dispersions can be outlined as follows: First, the nanoparticle dispersion is pumped through a nozzle, generating a fine mist that is then released into a heated chamber. In this chamber, the solvent in the individual droplets is evaporated and the nanoparticles are forced together. These dried droplets are further transported by airflow to a cyclone and can be collected in a vessel located at the bottom of the cyclone. In **Figure 2**, scanning electron microscopy (SEM) images of the different spray-dried silica-APTES-zinc samples are presented.

In the case of the silica-APTES sample, nearly spherical supraparticles were obtained (Figure 2 yellow box). This is due to homogenous water removal over the entire droplet surface upon evaporation forcing the large nanoparticle agglomerates to preferably center in the middle of the droplet due to their large sizes (**Scheme 2**, yellow box).[19,21,22] As the zinc concentration in the nanoparticle dispersion increases, the size of the agglomerates decreases, and the increasingly stable small nanoparticles disperse preferentially in the outer zone of the sprayed droplet. During evaporation, the dense nanoparticle shell obstructs a uniform water evaporation across the entire droplet surface, yet accelerates spontaneous water vaporization in certain surface areas because of localized cracking of the nanoparticle shell (Scheme 2, blue box).[22,23] As a result, this leads to the formation of more "buckled" supraparticles (**Figure 3**, blue box).

In addition, upon examination of SEM micrographs of the supraparticles at higher magnifications (Figure S3, Supporting Information), it appears that the distance between the individual

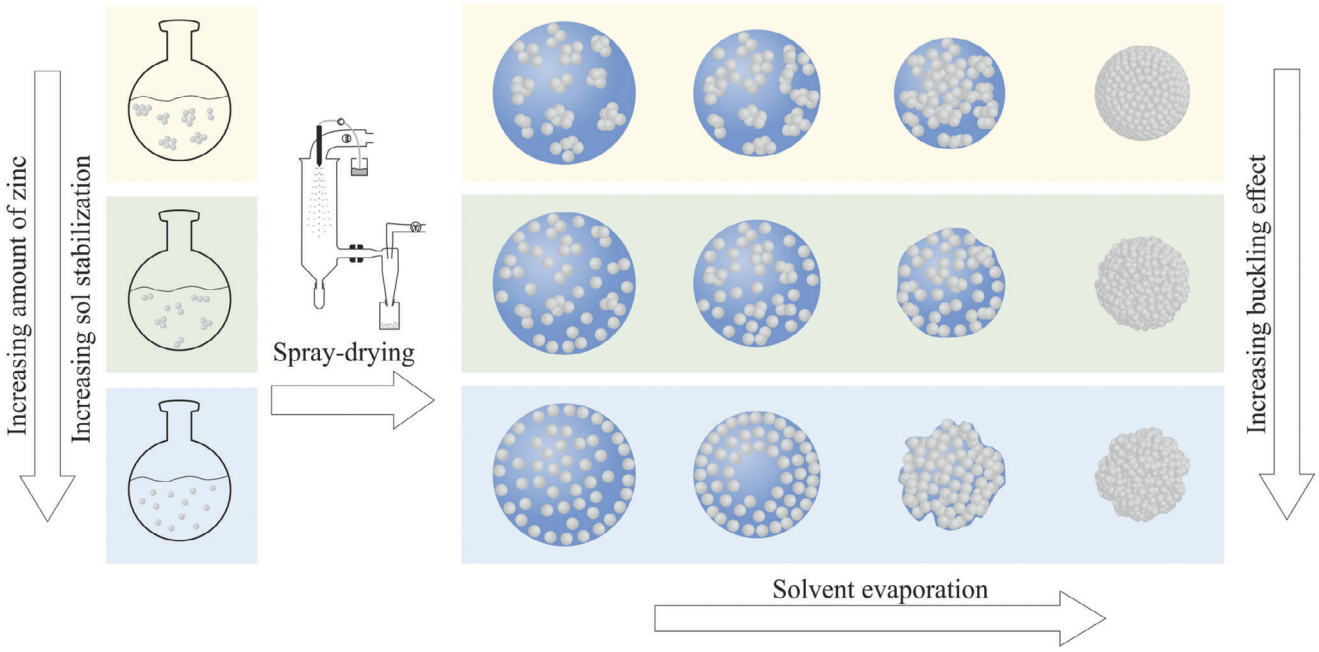

Scheme 2. Schematic illustration of the droplet formation and solvent evaporation during the spray-drying process of different stabilized silica-zinc nanoparticle dispersions resulting in more spherical or more buckled supraparticles. Samples without zinc (yellow), 40% zinc loading (green) and 100% loading (blue) are highlighted.

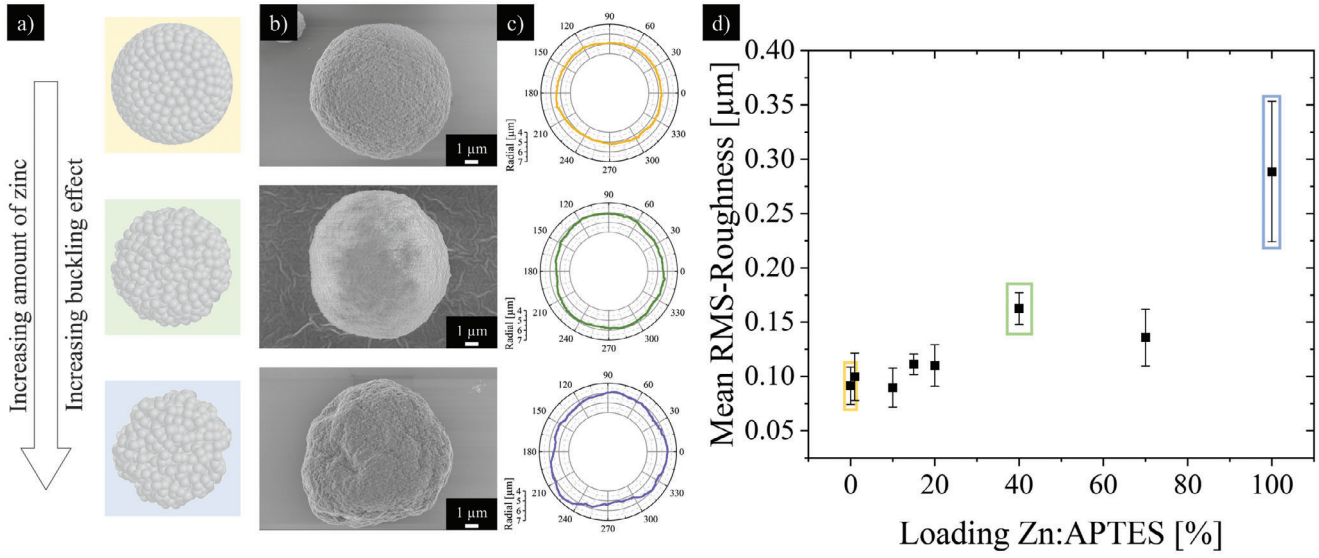

Figure 3. Investigation of the morphology of supraparticle with increasing zinc amount. Schematic display of the supraparticles without zinc (yellow), 40% zinc loading (green), and full loading (blue) a). High-resolution SEM images of the respective supraparticles b). The contour of the supraparticles plotted out of angularly resolved radii data c). Mean RMS-roughness, averaged out of three measurements, each for all supraparticles d).

nanoparticles decreases as the zinc concentration inclines, resulting in a reduced dispersion stability (i.e., pre-agglomeration declines). Consequently, the nanoparticles are more densely packed during spray-drying. Due to their improved stability in the dispersion (compare increased ζ-potential), the individual nanoparticles become more repulsive to each other, causing them to initially form a crust again. However, the APTES molecules on the surface create steric hindrance, preventing the individual nanoparticles from coming as close to each other as in the unmodified samples.

A Python code developed by Hülagü et al.[24,25] and subsequently modified by us[26] was used for the pixel-based automated calculation of supraparticle morphologies (Figure 3). Additional micrographs (of samples prepared on a Si-wafer instead of carbon pads) were taken to visualize the supraparticles' profiles using the same tool while aligning the focal plane with the surface of

the supraparticles (Figure 3b). The micrographs were converted into a binary format where pixels belonging to the supraparticles were shown as white, and the rest as black. Employing a Python code,[26] the supraparticles' boundary pixel was fixed as the interface between the white and black pixels. Once a boundary pixel was detected, its eight neighboring pixels were scrutinized to check if they were also a part of the boundary. A one-pixel wide border was found at the edge of the supraparticle pixels. The average of all identified boundary pixel values was utilized as the initial center of the supraparticle.[20] The distances (radii) from this initial center to all boundary pixels, as well as the standard deviation of these distances, were then calculated. The optimized center was determined by adjusting the initial center pixel-by-pixel in the x and y dimensions until the iterative calculation reached a minimum standard deviation. Using this optimized center, all boundary pixels were evaluated for their angularly resolved radii (Figure 3c). Formula (1) was used to calculate the RMS-roughness (root mean square-roughness) as the standard deviation of all radii.[24]

$$RMS-roughness = \sqrt{\frac{1}{N}\sum_{i=0}^{N} d_r^2} \quad (1)$$

The RMS-roughness was determined by calculating d_r, the radius from the optimized center to a boundary pixel, and N, the number of boundary pixels. At least three supraparticles were measured for their RMS-roughness, and the resultant values were averaged and reported as the mean RMS-roughness, complete with standard deviation (Figure 3d). From the silica-APTES-zinc-0% sample (marked in yellow) to the silica-APTES-zinc-20% sample, there was a gradual rise in the mean RMS-roughness, indicating values ranging between 90 and 111 nm and a standard deviation from 9 to 23 nm. These results suggest that no significant parameter for the formation of supraparticles was altered at zinc loadings of 20% or below. A noteworthy rise in the mean RMS-roughness with a minor standard deviation (163 ± 15 nm) was observed for silica-APTES-zinc-40% (marked in green), indicating changes in supraparticle formation. Conversely, silica-APTES-zinc-100% (highlighted in blue) exhibited a significant surge in both the mean RMS-roughness and its standard deviation (289 ± 64 nm), nearly doubling that of silica-APTES-zinc-40% (green) and more than tripling that of silica-APTES-zinc-0% (yellow). This correlation is supported by the overall impression of the buckling effect observed in the SEM micrographs (Figure 3b). Based on this consistent data, one can conclude that the Python code is a reliable approach to quantify the supraparticles' morphology in terms of the RMS-roughness of their profile.

To support these observations concerning nanoparticle dispersion stability, supraparticle morphology, and their correlation to inter-particle forces, results were compared to four additional reference samples (Figure S4, Supporting Information). As a first point of reference, pure silica nanoparticles that provide stable nanoparticle dispersions with high ζ-potential values, low hydrodynamic diameters, and low viscosity (ESI, part 4, Supporting Information) mainly form irregular, donut-shaped supraparticles (Figure S4a, Supporting Information). This phenomenon is due to the high stabilization and high negative ζ-potential of the pure silica nanoparticles in water. In the evaporation process, individual nanoparticles strongly repel each other, causing them to accumulate at the droplet's edge.[21,22,27] As the droplet shrinks, a crust forms, hindering water evaporation. Eventually, the crust collapses, allowing total evaporation and the formation of donut-shaped supraparticles. Compared to the silica-APTES-zinc-100% sample that exhibits comparable low agglomerate sizes, high ζ-potential, and low viscosity, the nanoparticles do not carry the respective "bulky" organic surface groups, resulting in the formation of a denser crust. This, in turn, is presumed to promote solvent evaporation in a specific spot rather than in several locations. This could explain the more donut-like morphology instead of a buckled morphology for the pure silica dispersion and *vice versa* for the silica-APTES-zinc-100% sample. In the second reference experiment, the pure silica nanoparticles were mixed with the same amount of zinc nitrate as the 100% silica-APTES-zinc sample to investigate the influence of the zinc salt on the supraparticle formation in the absence of zinc complexation (Figure S4b, Supporting Information). Compared to the pure silica supraparticles, no significant difference in morphology is observed, confirming the main role of zinc in modifying the silica surface properties. In the third reference, zinc nitrate is replaced by sodium nitrate using the silica-APTES nanoparticles. Since sodium cannot be complexed by the APTES amino groups, the resulting supraparticles are as spherical as the pure silica-APTES-zinc-0% sample (Figure S4c, Supporting Information). In the fourth reference experiment, silica-APTES nanoparticles and zinc nitrate were spray-dried using a three-fluid nozzle. This minimized the possible reaction time for the complexation process of zinc nitrate and the amine groups, as they only came into contact with the individual droplets. This resulted in the collection of supraparticles with sphericity similar to silica-APTES-zinc-0% but with zinc crystals on their surface (Figure S4d, Supporting Information). In summary, these three reference experiments confirm that zinc is complexed by the amine surface groups of the nanoparticles and thus dominates their agglomeration state and surface charge, which ultimately influences the obtained supraparticle morphology.

To ensure optimal redispersion behavior, we consider supraparticles with the highest zinc content to be the sample of choice. Due to the more curved and rough morphology of the supraparticles, mechanical deformation should be easier than for perfectly spherical samples. Additionally, the hydrogen bonds between the amine groups in the samples with the lower zinc concentration cause stronger bonding between the individual nanoparticles, resulting in a more stable supraparticle. In contrast, in the sample with the highest zinc concentration, hydrogen bonds are absent, and repulsive forces act between the Zn^{2+} atoms.

In order to investigate the potential use of the zinc single-site anchored silica nanoparticles in the form of supraparticles for the vulcanization process of IR, an upscaled batch of these building blocks was synthesized (see Experimental Section). Apart from safety considerations, no special adaption to the protocol had to be carried out for upscaling the synthesis procedure of silica-APTES-zinc-100%. The initial half of the obtained batch was centrifuged and oven dried, according to the standard literature protocol as reference material, denoted as "silica-APTES-zinc-100% nanoparticles oven dried" in the following. The second part was utilized to prepare supraparticles. For upscaling purposes, a two-fluid nozzle was used instead of the previously utilized ultrasonic

Table 1. Composition of rubber composites.

Ingredients	Amount (parts per hundred rubber, phr)
IR	100
SiO_2 filler	54.0
TESPD compatibilizing agent*	4.3
6-PPD antioxidant	2.0
ZnO*	1.0
Stearic acid co-activator*	2.0
CBS accelerator	1.6
S_8	3.0

*TESPD, ZnO, and stearic acid were used only for the reference silica+ZnO/IR nanocomposite.

nozzle to increase the product yield. This change generally does not affect supraparticle morphologies but only decreases their size.[28] The resulting sample is denoted as "silica-APTES-zinc-100% supraparticles". These materials were then used to prepare silica/IR nanocomposites, acting both as a curing activator and a reinforcing filler. The nanocomposites were compared to a standard reference nanocomposite prepared using bare silica nanoparticles and microcrystalline zinc oxide, traditionally used in industrial applications, with the addition of TESPD as a compatibilizing agent (see **Table 1** for the composition of the rubber composites). The vulcanization curves of IR nanocomposites were recorded at 170 °C for 5 min, by measuring the torque (S') over curing time. This treatment promotes the formation of sulfur cross-links between the rubber chains, leading to a more viscous material and an increase in registered S' values. Subsequent vulcanization tests were conducted using the two aforementioned samples and a standard reference sample based on silica and zinc oxide, which is also commonly used in the industry. The study of the vulcanization mechanism and of the interactions between the Zn(II) centers supported over silica nanoparticles and the other curing agents was performed in our previous work.[13] **Figure 4** displays the measured vulcanization curves of the three samples (reference, silica-APTES-zinc-100% nanoparticles oven dried, silica-APTES-zinc-100% supraparticles). The typical S-shaped vulcanization curves indicate a catalytically activated curing. The differing curve progression in the case of the IR containing silica-APTES-zinc nanoparticles, suggests that possibly only a thermal curing process is promoted. Among them, the silica-APTES-zinc supraparticles exhibit superior performance in the vulcanization process of IR nanocomposites. They demonstrate a lower scorch time (time to reach the first incipience of cross-linking), higher maximum torque S' values, and lower curing time (time to reach the maximum torque value) compared to both, the reference sample and the respective oven-dried nanoparticles. The curing parameters are reported in Table S2 (Supporting Information). This suggests that the individual zinc sites have high catalytic activity over the supraparticles and are highly available to promote the curing process in the overall rubber matrix. The supraparticle sample exhibits higher activity compared to microcrystalline zinc oxide, which is consistent with a higher amount of accessible zinc due to the significantly lower specific surface area of zinc oxide compared to its molecular counterpart.[13] Additionally, the improved vulcanization efficiency when compared to the oven-dried nanoparticle sample suggests a more homogenous distribution of the supraparticles in the rubber matrix, resulting in a better interaction with the other vulcanizing agents and leading to a more homogeneous network formation. In the case of IR containing silica-APTES-zinc nanoparticles, the poor distribution of silica nanoparticles in the matrix due to the large and hard agglomerates formed during the drying process reduces the availability of Zn(II) active sites and drastically decreases the overall curing efficiency, resulting in the formation of a long marching cure curve. Also, measurements were taken to determine the dynamic mechanical behavior of the three rubbers vulcanized using the different zinc samples (Figure S5, Supporting Information). Here, the higher values of the elastic modulus G' combined with the lower values of tan δ of the sample vulcanized using supraparticle confirm its higher mechanical performance compared to the other samples. The homogeneous distribution of the silica filler in the polymer matrix can explain this phenomenon. The supraparticles redisperse down to the nanoscale during the compounding process, resulting in better filler incorporation into the network and, consequently, improved filler-rubber interaction.

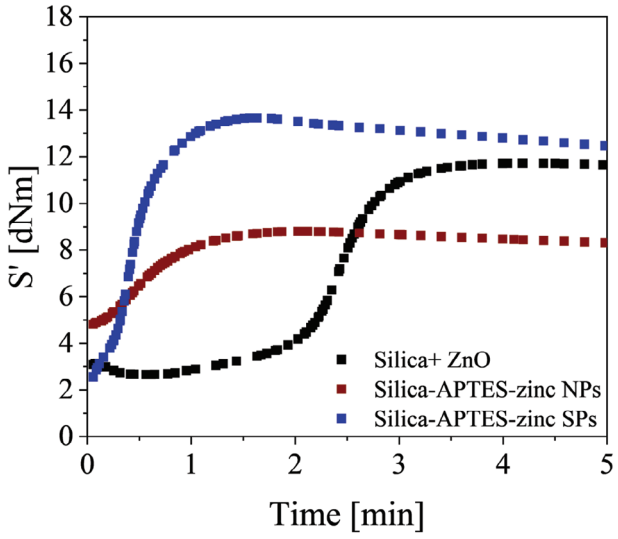

Figure 4. Vulcanization curves of a standard reference IR nanocomposite (black), and IR nanocomposites prepared with silica-APTES-zinc-100% nanoparticles dried in an oven (red) and respective supraparticles (blue).

In order to examine the distribution behavior of the oven-dried agglomerated nanoparticles in comparison to the supraparticle sample, cross-section SEM images of the rubber samples were acquired (**Figure 5**). The rubber sample containing oven-dried nanoparticles exhibits an inhomogeneous distribution of large nanoparticle agglomerates (Figure 5-a1). In the higher magnification images (Figure 5-a2), only a few nanoparticle oligomers are clearly distinguishable in the matrix, while most of them are present as hard agglomerates, preventing the formation of a homogeneous filler network. However, in the case of the supraparticle sample, however, the supraparticle structure was disrupted (Figure 5-b1) due to the mixing process, resulting in a homogeneous distribution of smaller nanoparticle oligomers throughout the sample (Figure 5-b2). SEM images of the standard

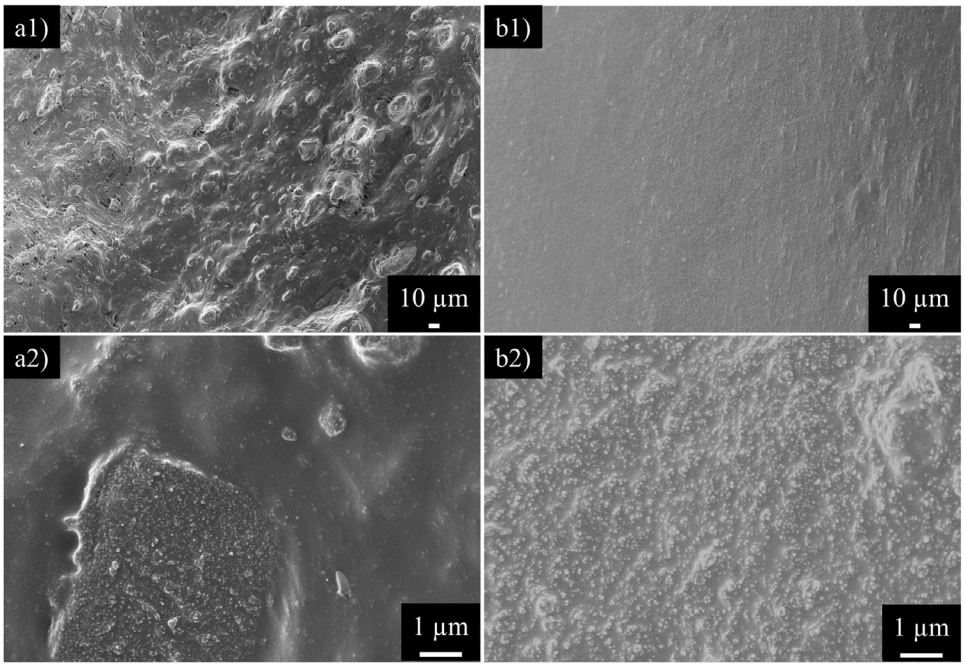

Figure 5. SEM images of silica-APTES-zinc nanoparticles dried in an oven and incorporated in rubber a), as well as redispersed, spray-dryed silica-APTES-zinc supraparticles in the rubber matrix b). An overview is shown in 1) as well as a higher magnification of the respective samples in 2).

reference sample incorporated into the rubber matrix are shown in the Figure S6 (Supporting Information).

3. Conclusion

This work presents a more sustainable and environmentally friendly synthesis for the preparation of zinc single sites anchored on silica nanoparticles, as described in the literature. The solvent toluene, as well as reflux conditions, were avoided during particle functionalization reactions. Additionally, the free-flowing powder required for the nanoparticle integration into rubber was produced using spray-drying, which yields so-called supraparticles. The surface modification of silica nanoparticles allows the resulting supraparticles to almost completely disintegrate into primary particles during the vulcanization process. This leads to improved cure behavior and dynamic mechanical properties of superparticles-containing rubber compared to those with oven-dried nanoparticles or traditional zinc oxide catalysts. During the experiments, the influence of zinc concentration on the morphology of the obtained supraparticles was observed and further investigated as the core of this study. At low zinc concentrations, attractive forces in the form of hydrogen bonds between the amine molecules dominate. This results in a destabilized nanoparticle dispersion and consequently more spherical supraparticles upon spray-drying. The more zinc is present in the sample, the stronger are the repulsive forces between the zinc atoms and thus, between the individual nanoparticles. This outweighs the attractive forces between the amino groups, leading to the formation of supraparticles with a more buckled morphology due to a more stabilized nanoparticle dispersion. In summary, this study successfully elucidated the role of zinc ions and their amino-complexation in nanoparticle dispersion stability as well as their role in supraparticle formation during spray-drying. Additionally, the study demonstrated the superior performance of such zinc single site-containing silica supraparticles as catalysts in rubber vulcanization.

4. Experimental Section

The chemicals were used without further purifications and purchased from the following companies: ethanol (Jäckle-Chemie, Germany), (3-aminopropyl)triethoxysilane (APTES, Sigma–Aldrich, Germany), tetraethoxysilane (TEOS, Sigma–Aldrich, Germany), aqueous ammonia solution (NH_3(aq), 25%, Merck, Germany), zinc nitrate hexahydrate ($Zn(NO_3)_2{\cdot}6H_2O$, Sigma–Aldrich, Germany). All experiments were performed with deionized water. Dialysis was performed by using a cellulose acetate membrane with a molecular-weight cut-off of 10 kDa against water with several water exchanges. For IR nanocomposites: cis-1,4-polyisoprene rubber (IR) (Nizhnekamskneftekhim Export, Russia), bis(3-triehoxysilylpropyl)disulfide (TESPD, Sigma–Aldrich, Germany), antioxidant N-(1,3-dimethylbutyl)-N-phenyl-phenylenediamine (6-PPD, Flexsys, USA). The curing agents were: stearic acid (Undesa, USA), ZnO (wurtzite, Zincol Ossidi, Italy), N-cyclohexyl-2-benzothiazole sulfenamide (CBS, Lanxess, Italy), sulfur Creso (Redball, Superfine, USA).

Synthesis and Modification of Silica Nanoparticles: Silica nanoparticles were synthesized according to the protocol of Stöber et al.[18] Therefore, 791 g of ethanol were mixed with 50 g of an aqueous ammonia solution and heated up to 40 °C. Under vigorous stirring, 50 g of TEOS were added and the mixture was allowed to stir for minimum 12 h. After cooling to room temperature 1468 µL of APTES were added to reach a theoretical functionalization degree of 100% regarding the calculated amount of available OH groups.[19,20] After further 24 h of stirring at room temperature, the particles were purified using an evaporation process and dialysis. After determination of the actual APTES concentration by TGA analysis and the weight percentage of modified silica nanoparticles by gravimetric analysis, the batch was divided in eight fractions and mixed with $Zn(NO_3)_2{\cdot}6H_2O$ in different amounts to reach an occupancy degree of the anchored APTES groups of 0, 1, 10, 15, 20, 40, 70, and 100% (Table S1, Supporting Information, where 100% is the maximum zinc loading, corresponding to

Zn:APTES coordination equal to 1:2) and the mixtures were stirred again over night.

Spray-Drying Process: Without further purification, the modified silica nanoparticles were spray-dried using a B290 laboratory spray-dryer (Büchi, Switzerland). The inlet temperature was set to 140 °C, the aspirator power to 75% and the pump rate to 15%. An ultrasonic nozzle was used with a power of 5 W.

Upscaling Process: To perform the vulcanization experiments in rubber nanocomposites larger amount of modified silica nanoparticles were prepared. Therefore, 9.85 kg of ethanol were mixed with 627.9 g of an aqueous ammonia solution in a 100-L-batch reactor (Büchi, Switzerland) and heated up to 30 °C. Under stirring, 693.5 g TEOS were added and the mixture was allowed to stir over night. After cooling to room temperature, 252.8 g of APTES were added and the mixture was again stirred overnight. The purification of the modified nanoparticles was done by rotary evaporation, following by centrifugation. After three washing steps with water the batch was divided in two parts, one as reference for the rubber compounding experiments and one for further modification with zinc. Each batch has a silica concentration of about 92 g, determined by gravimetric analysis. The first batch was spray-dried using a two-fluid nozzle to minimize the yield loss, an inlet temperature of 140 °C, an aspirator power of 100%, and a pump rate of 20%. The second batch was mixed with 17 g of $Zn(NO_3)_2{\cdot}6H_2O$ (corresponding to zinc loading equal to the 100% sample), stirred overnight, and dried in an oven.

Characterization: The characterization of the nanoparticle dispersion as well as for the supraparticles was done using different techniques. The hydrodynamic particle diameter of the silica nanoparticles was measured using a ZetaSizer ZS (Malvern Instruments, United Kingdom) to determine the particle size. Triplicate measurements were done with minimum 12 measurements per run at 25 °C.

The kinematic viscosity of the nanoparticle dispersions was determined using a capillary viscosimeter (CT 050, AVS 400, CK 100, Schott, Germany) with a glass ubbelohde capillary with a constant of 0.02908. The measurements were performed at 25 °C and in fivefold runs.

The morphology and the sphericity investigation of the supraparticles was done using a Supra 25 SEM (Zeiss, Germany) at 2 kV (field emission). For the sphericity investigations, an inlense detector was used and the particles were prepared on a Si-wafer. The focal plane was aligned with the particle profile and high-resolution images (3072 × 2304 pixels) were obtained. Using the Fiji software (2.0.0-rc-49/1.51d/Java 1.8.0_66), the pixel length of the scalebar was determined and the image was cropped to display only the desired supraparticle. Also using Fiji, the image was binarized using the threshold function, and noise pixels were removed via the remove outliers function. Pixels attributed to the supraparticles were contributed to the foreground and displayed as white, pixels attributed to the background were displayed as black. The edited image was analyzed for the radii resolved by angle and RMS-roughness using a Python code (Spyder 5.4.1, Anaconda Navigator 1.10.0), which can be found online.[26] The used Python code was a modified version of the code created by Hülagü et al.[24,25]

Rubber Composites and Vulcanization Tests: The ingredients were mixed in a Brabender Plasti-Corder lab station internal mixer (Brabender GmbH & Co. KG, Germany) (65 mL mixing chamber, 0.6 filling factor, 60 rpm rotor speed). All IR nanocomposites were prepared by keeping a constant zinc content (1 parts per hundred, phr) and silica content (54 phr). In the first phase, IR was masticated into the mixing chamber at 90 °C and mixed with silica-APTES-Zn nanoparticles oven-dried (or supraparticles) and antioxidant 6-PPD (2 phr). 3 min of mixing are required for the filler incorporation in IR. In the second phase, after reloading the composites into the mixer at 90 °C, CBS (1.6 phr) and S_8 (3.0 phr) were added. Lastly, a two-roll mill (50 °C, 3 min) was employed to improve the nanocomposite homogeneity. Reference silica+ZnO/IR nanocomposite were prepared using conventional microcrystalline ZnO as a curing activator and as prepared silica nanoparticles (Stöber method). Nanocomposites were produced with a similar procedure to that previously described. However, in the first step, bare silica nanoparticles (54 phr), TESPD compatibilizing agent (4.3 phr), 6-PPD (2.0 phr), ZnO (1.0 phr), and the coactivator stearic acid (2.0 phr) were mixed with IR at 145 °C. The higher temperature was required for the silica-combatilizer interaction. All rubber composites were prepared at a constant zinc content equal to 1.0 phr.

The vulcanization curves and the dynamic mechanical properties were registered by a rubber process analyzer (RPA2000, Alpha Technologies). The composites were vulcanized at 170 °C and 100 bar for 5 min (frequency = 1.670 Hz, angle = 6.980°). The dynamic mechanical properties were studied by applying a shear stress mode. The strain sweep tests were carried out at 70 °C and 10 Hz, at angle values between 0% and 10%. Specimens were cut using a rubber sample cutter (CUTTER2000, Alpha Technlogies, Germany, weight = 5.0 ± 0.3 g). Two measurements were carried out for each sample, and the average value was reported.

Supporting Information

Supporting Information is available from the Wiley Online Library or from the author.

Acknowledgements

The authors thanks Hanna Gast and Selina Kosdik for supporting in the silica nanoparticle synthesis and Doris Hanselmann for supporting in the upscaling procedure. P.M. thanks the CORIMAV (Consortium for the Research of Advanced Materials between Pirelli and University of Milano Bicocca) for its support within the PCAM European Doctoral Program.

Conflict of Interest

The authors declare no conflict of interest

Author Contributions

General research goals were developed by S.W., P.M., S.M., R.S., S.Wi, and K.M. The supervision of the whole project was done by S.W., R.S., S.W., and K.M. Performance of the syntheses and characterizations were carried out by S.W., P.M, J.P., and M.O. Interpretation and conclusion of the results were conducted by S.We. in discussion with T.Z, M.O., S.W., and K.M. Interpretation on the vulcanization results was done by P.M., S.M., and R.S. RMS-roughness was determined and interpreted by T.Z. with support of M.D. Figures were created by S.W. The original manuscript draft was written by S.We. with the contribution of T.Z and S.Wi. Reviewing and editing were performed by S.We., P.M., T.Z., S.M., R.S., S.W., and K.M. All authors proof-read and commented on the publication.

Data Availability Statement

The data that support the findings of this study are available in the supplementary material of this article.

Keywords

morphology control, rubber nanocomposite, silica nanoparticles, spray-dried supraparticles, surface modification, zinc-activated vulcanization

Received: October 17, 2023
Revised: December 20, 2023
Published online:

[1] "https://de.statista.com/statistik/daten/studie/223866/umfrage/reifenproduktion-in-europa/" (accessed: June 2023).

[2] a) H. Xu, X. Fan, Y. Song, Q. Zheng, *Compos. Sci. Technol.* **2020**, *187*, 107943; b) L. Chen, L. Wu, L. Song, Z. Xia, Y. Lin, W. Chen, L. Li, *Nanoscale* **2020**, *12*, 24527.
[3] J. Kruželák, R. Sýkora, I. Hudec, *Chem. Pap.* **2016**, *70*, 1533.
[4] a) P. Ghosh, S. Katare, P. Patkar, J. M. Caruthers, V. Venkatasubramanian, K. A. Walker, *Rubber Chem. Technol.* **2003**, *76*, 592; b) D. Spence, J. D. Ferry, *Rubber Chem. Technol.* **1938**, *11*, 47; c) G. Heideman, R. N. Datta, J. W. M. Noordermeer, B. van Baarle, *J. Appl. Polym. Sci.* **2005**, *95*, 1388.
[5] a) L. M. García Rojas, C. A. Huerta-Aguilar, E. D. Tecuapa-Flores, D. S. Huerta-José, P. Thangarasu, J. S. Sidhu, N. Singh, M. de La Luz Corea Téllez, *J. Mol. Liq.* **2020**, *319*, 114107; b) A. Moezzi, A. M. McDonagh, M. B. Cortie, *Chem. Eng. J.* **2012**, *1*, 185.
[6] S. Mostoni, P. Milana, B. Di Credico, M. D'Arienzo, R. Scotti, *Catalysts* **2019**, *9*, 664.
[7] a) T. B. Councell, K. U. Duckenfield, E. R. Landa, E. Callender, *Environ. Sci. Technol.* **2004**, *38*, 4206; b) E. P. Rhodes, Z. Ren, D. C. Mays, *Environ. Sci. Technol.* **2012**, *46*, 12856.
[8] a) X. Qin, H. Xu, G. Zhang, J. Wang, Z. Wang, Y. Zhao, Z. Wang, T. Tan, M. R. Bockstaller, L. Zhang, K. Matyjaszewski, *ACS Appl. Mater. Interfaces* **2020**, *12*, 48007; b) B. Panampilly, S. Thomas, *Polym. Eng. Sci.* **2013**, *53*, 1337; c) T. K. Sreethu, M. Das, A. R. Parathodika, A. B. Bhattacharya, K. Naskar, *J. Appl. Polym. Sci.* **2023**, *140*, e53257.
[9] a) M. Maciejewska, A. Sowińska, A. Grocholewicz, *Materials* **2021**, *14*, 3804; b) M. Maciejewska, A. Sowińska, J. Kucharska, *Polymers* **2019**, *11*, 1723; c) P. Junkong, R. Morimoto, K. Miyaji, A. Tohsan, Y. Sakaki, Y. Ikeda, *RSC Adv.* **2020**, *10*, 4772.
[10] a) Z. Yang, Y. Huang, Y. Xiong, *RSC Adv.* **2020**, *10*, 41857; b) Y. Li, J. Wu, Q. Zhang, F. Dong, Y. Xiong, *Ind. Eng. Chem. Res.* **2020**, *59*, 4493.
[11] a) M. N. Alam, V. Kumar, P. Potiyaraj, D.-J. Lee, J. Choi, *J. Elastom. Plast.* **2022**, *54*, 123; b) S. M. Javadi, *Curr. Biochem. Eng.* **2020**, *6*, 103.
[12] a) M. Hussain, S. Yasin, M. Adnan Akram, H. Xu, Y. Song, Q. Zheng, *Ind, Eng. Chem. Res.* **2019**, *58*, 18205; b) M. Maciejewska, A. Sowińska, *Polymers* **2021**, *13*, 1656; c) A. Sowińska, M. Maciejewska, A. Grajewska, *Int. J. Mol. Sci.* **2021**, *22*, 3678; d) M. A. Sattar, A. Patnaik, *Chem. Sus. Chem.* **2023**, *16*, e202202309; e) M. A. Sattar, *Chem. Sus. Chem.* **2023**, *17*, e202301001.
[13] S. Mostoni, M. D'Arienzo, B. Di Credico, L. Armelao, M. Rancan, S. Dirè, E. Callone, R. Donetti, A. Susanna, R. Scotti, *Ind. Eng. Chem. Res.* **2021**, *60*, 10180.
[14] A. Susanna, L. Armelao, E. Callone, S. Dirè, M. D'Arienzo, B. Di Credico, L. Giannini, T. Hanel, F. Morazzoni, R. Scotti, *Chem. Eng. J.* **2015**, *275*, 245.
[15] S. Mostoni, P. Milana, C. Marano, L. Conzatti, M. Mauri, M. D'Arienzo, B. Di Credico, R. Simonutti, P. Stagnaro, R. Scotti, *Compis. Sci. Technol.* **2022**, *230*, 109780.
[16] S. Wintzheimer, T. Granath, M. Oppmann, T. Kister, T. Thai, T. Kraus, N. Vogel, K. Mandel, *ACS Nano* **2018**, *12*, 5093.
[17] C. Stauch, T. Ballweg, W. Stracke, R. Luxenhofer, K. Mandel, *J. Colloid Interf. Sci.* **2017**, *490*, 401.
[18] W. Stöber, A. Fink, E. Bohn, *J. Colloid Interf. Sci.* **1968**, *26*, 62.
[19] S. Wenderoth, T. Granath, J. Prieschl, S. Wintzheimer, K. Mandel, *Adv. Photo. Res.* **2020**, *1*, 2000023.
[20] L. T. Zhuravlev, *Colloid Surface A* **2000**, *173*, 1.
[21] S. Wenderoth, G. Bleyer, J. Endres, J. Prieschl, N. Vogel, S. Wintzheimer, K. Mandel, *Small* **2022**, *18*, e2203068.
[22] A. B. D. Nandiyanto, K. Okuyama, *Adv. Powder Technol.* **2011**, *22*, 1.
[23] a) H. Zhou, R. Pujales-Paradela, P. Groppe, S. Wintzheimer, K. Mandel, *Part. Part. Syst. Charact.* **2022**, *39*, 2200127; b) Y. Huang, S. Yan, S. Zhang, Q. Yin, X. Chen, W. D. Wu, *Colloid Surface B* **2022**, *217*, 112610.
[24] D. Hülagü, C. Tobias, E. Climent, A. Gojani, K. Rurack, V.-D. Hodoroaba, *Adv. Eng. Mater.* **2022**, *24*, 2101344.
[25] "GitHub Repository for the Python Code", can be found under https://github.com/BAMresearch/Roughness-Analysis-by-Electron-Microscopy (accessed: September **2022**).
[26] "GitHub Repository for the Python Code", can be found under https://github.com/ThomasZimmermannFAU/Pixel-based-Roughness-Analysis-from-Microscopy-Images (accessed: September **2023**).
[27] F. Iskandar, L. Gradon, K. Okuyama, *J. Colloid Interf. Sci.* **2003**, *265*, 296.
[28] a) F. Miller, S. Wenderoth, S. Wintzheimer, K. Mandel, *Adv. Opt. Mater.* **2022**, *10*, 2201642; b) R. Vehring, H. Snyder, D. Lechuga-Ballesteros, in *Drying Technologies for Biotechnology and Pharmaceutical Applications*, (Eds.: S. Ohtake, K. Izutsu, D. Lechuga-Ballesteros), Wiley, Hoboken, NJ **2020**, 179.

